

**Interplay of Structural Fluctuations and Charge Carrier  
Dynamics is Key for High Performance of Hybrid Lead Halide  
Perovskites**

Journal:	<i>Inorganic Chemistry Frontiers</i>
Manuscript ID	QI-RES-07-2022-001482.R1
Article Type:	Research Article
Date Submitted by the Author:	17-Aug-2022
Complete List of Authors:	Zhan, Juan; Hunan Agricultural University; Hunan Agricultural University; Hunan Agricultural University Yang, Jack; University of New South Wales , School of Material Science and Engineering Xie, XIAoyin; Hubei Polytechnic University Prezhdo, Oleg; University of Southern California, Chemistry Li, Wei; Hunan Agricultural University, School of Chemistry and Materials Science

# Interplay of Structural Fluctuations and Charge Carrier Dynamics is Key for High Performance of Hybrid Lead Halide Perovskites

Juan Zhan,<sup>1</sup> Jack Yang,<sup>2</sup> Xiaoyin Xie,<sup>3\*</sup> Oleg V. Prezhdo,<sup>4\*</sup> and Wei Li<sup>1\*</sup>

<sup>1</sup>*School of Chemistry and Materials Science, Hunan Agricultural University, Changsha 410128, China*

<sup>2</sup>*School of Material Science and Engineering, Materials and Manufacturing Futures Institute, University of New South Wales, Sydney, New South Wales 2052, Australia*

<sup>3</sup>*School of Chemistry and Chemical Engineering, Hubei Polytechnic University, Huangshi, 435003, China*

<sup>4</sup>*Department of Chemistry, University of Southern California, Los Angeles, California 90089, United States*

E-mails:

[xyxie@hbpu.edu.cn](mailto:xyxie@hbpu.edu.cn) (X.Y.X.);

[prezhdo@usc.edu](mailto:prezhdo@usc.edu) (O.V.P.);

[weili@hunau.edu.cn](mailto:weili@hunau.edu.cn) (W.L.)



## Abstract

The ability of methylammonium lead triiodide (MAPbI<sub>3</sub>) to achieve photoelectric conversion efficiency that is on par with crystalline silicon has led to a surge of interest in perovskite photovoltaics. However, an in-depth understanding of how the ubiquitous coupling between the fast rovibrational movements of the organic cations and the phonon vibrations of the inorganic framework affects the relaxation and recombination of hot carriers remains largely elusive. Access to such knowledge is critical to guide design and increase efficiency of new classes of perovskite solar cells. We report a time-domain *ab initio* investigation of temperature dependent excited state dynamics in MAPbI<sub>3</sub>, with particular emphasis on nuclear anharmonic effects. The observed strong anharmonicity is attributed to softness of the material and unusual dynamical coupling between the organic and inorganic components. At an elevated temperature, the hydrogen bonding between MA and iodines is weakened, enhancing rotation of MA cations, which become more dynamically disordered. As a result, thermal vibrations of the inorganic Pb-I sublattice are suppressed, and the lattice anharmonicity is decreased. Thermal fluctuations of the electronic energy levels are found to follow the trend of anharmonic motions of Pb and I atoms, with holes relaxing faster to the band edges than electrons, due to higher density of the hole states. While elevated temperature accelerates intraband carrier cooling, it slows nonradiative carrier recombination. The latter result is important for performance, since solar cells and other devices heat up during operation. The reported signatures of coupled structural dynamics of the organic cations and inorganic framework unravel the interplay between anomalous structural fluctuations and charge carrier dynamics, which is of particular importance for fundamental understanding of the structure-property relationships in hybrid metal halide perovskites.

## 1. Introduction

Hybrid organic-inorganic perovskites have been identified as one of the most promising materials in energy-related and optoelectronic devices owing to their low-cost and excellent optoelectronic properties, such as high absorption coefficients, bandgap tunability, micrometer carrier diffusion length, ambipolar transport characteristics, and slow charge recombination.<sup>1-7</sup> The record conversion efficiency of perovskite solar cells (PSCs) based on methylammonium lead iodide (MAPbI<sub>3</sub>) has exceeded 25%, approaching the conversion efficiency of single-crystalline silicon (~27%).<sup>8</sup> However, further improvements in the PSCs efficiencies have seen limited breakthrough in the recent years. The underlying physical limitations behind this slow progress are not sufficiently understood. Fundamentally, the intra- and inter-band carrier relaxations are the two key energy loss channels that determine the efficiency of a solar cell. The former corresponds to the relaxation of hot carriers toward the band edges, while the latter usually refers to the recombination of band edge carriers (electrons and holes) across the bandgap. Figure 1 provides an illustration of these processes. Both processes can reduce the carrier lifetime and transfer electronic energy to the lattice through inelastic carrier-phonon interactions. Higher solar cell efficiencies can be achieved if these two energy loss pathways are suppressed. To drive efficiencies of the PSCs toward the Shockley-Queisser limit and beyond, atomistic understanding of the photo-physical processes in hybrid perovskites is of fundamental interest, since most of the work has been focusing on the material fabrication and device optimization.<sup>9</sup>

Extensive investigations have been carried out to study the charge carrier dynamics in metal halide perovskites (MHPs).<sup>10-17</sup> Experimentally, most of the photophysical studies are based on time-resolved spectroscopy measurements. Sub-picosecond hot carrier cooling<sup>18</sup> and nanosecond electron-hole recombination<sup>2</sup> in MAPbI<sub>3</sub> have been identified. These timescales are much slower than those in

the conventional semiconductors, such as Si and GaAs,<sup>19</sup> partly accounting for the superior optoelectronic properties of MHPs. In order to understand the origin of long carrier lifetime, considerable efforts have been devoted to elucidate the nature of the characteristic dynamic structure of MHPs by using various techniques.<sup>20</sup> Nevertheless, fundamental understanding of the interplay of dynamic structure fluctuation and charge carrier dynamics in MHPs still remain as a challenge, motivating the detailed atomistic understanding of the kinetics of the nonequilibrium processes at the operational temperatures.

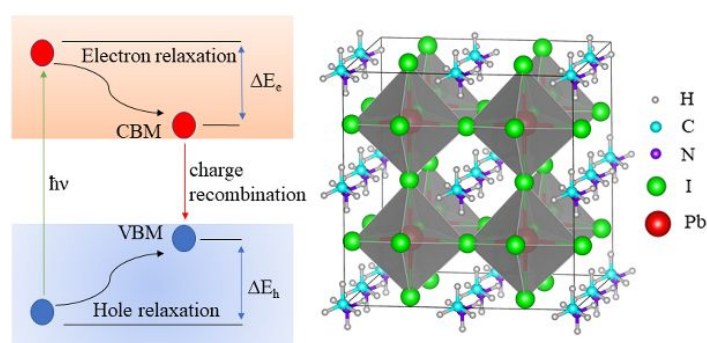


**Figure 1.** Schematic of relaxation of hot electrons and holes to the band edges, and nonradiative electron-hole recombination across the bandgap (**left**). Atomic structure of the MAPbI<sub>3</sub> perovskite crystal (**right**). The shaded grey region represents the [PbI<sub>6</sub><sup>4-</sup>] octahedra.

Here, we systematically explore the effect of temperature on the charge carrier relaxation in MHPs, with emphasis on the intrinsic anharmonicity of the perovskite lattice and the interplay between the organic cations and the inorganic network. This is achieved through using a combination of nonadiabatic molecular dynamics (NA-MD) and time-domain density functional theory (TD-DFT). By focusing on the cooling of hot electrons and holes, as well as the nonradiative electron-hole recombination processes, we show that elevated temperature enhances the rotation of MA cations,

which subsequently “locks” the fluctuations of the Pb-I lattice. Based on the analysis using the recently proposed anharmonic score, we observe a strong anharmonicity in the MAPbI<sub>3</sub> perovskite, which can be attributed to the coupling between rotational motions of the organic cations and fluctuations of the inorganic sublattice. Inorganic Pb and I atoms exhibit weaker anharmonicity at higher temperature because of the suppressed tilting of the inorganic [PbI<sub>6</sub><sup>4-</sup>] octahedra. The hydrogen-bonding interactions between the MA cations and the iodine in the lattice are weakened at higher temperature, since MA cations in the lattice become dynamically disordered, rotating in an isotropic potential. Electronic structure calculations indicate that thermal fluctuations of electronic energy levels follow the same trend as the anharmonic score, induce changes in the NA couplings (NACs), and correspondingly alter the rates of intra- and inter-band transitions of charge carriers at different temperatures.

## 2. Computational Methodology

The NA-MD simulations are performed with the mixed quantum-classical fewest switches surface hopping (FSSH)<sup>21</sup> and decoherence-induced surface hopping (DISH)<sup>22</sup> algorithms within the framework of TD-DFT in the Kohn-Sham representation, as implemented in the PYXAID code.<sup>23,24</sup> Heavier nuclei are treated (semi)-classically, whereas lighter electrons are described quantum mechanically. FSSH has been the most popular NA-MD algorithm, and is stable and accurate when modeling rapid transitions within dense manifold of states in nanoscale systems,<sup>25–29</sup> such as the intra-band carrier relaxation discussed herein. Slow quantum transitions involving few states with well-

separated energy levels, i.e., the electron-hole recombination across the fundamental gap, require incorporation of decoherence effects, since straightforward quantum-classical treatment overestimates the recombination rate. Introduction of decoherence by means of stochastic collapse of wave-function into adiabatic states provides the physical mechanism for surface hopping, leading to the DISH scheme.<sup>22</sup> The NA-MD simulations based on the FSSH and DISH schemes have been widely used to model carrier relaxation and recombination in a broad range of nanoscale systems.<sup>30-37</sup>

The FSSH algorithm is more established, tested and used than the DISH method. However, FSSH overestimates rates for transitions across large energy gaps. DISH includes decoherence effects and makes the interband transitions slower, in agreement with experiment. DISH can be used to study intraband relaxation as well, however, its reliability in such situations requires further studies. In particular, transitions within dense manifolds of states occur faster than loss of coherence between corresponding states. However, DISH transitions happen at decoherence events. Detailed balance between transitions upward and downward in energy is considered in DISH when transitions take place, i.e., also at decoherence events. Because decoherence between nearly degenerate states is slow, DISH appears to overestimate intraband relaxation times. Transitions are not frequent enough, and detailed balance responsible for the overall flow of electronic populations downward in energy is not considered sufficiently frequently. This problem does not arise in the stochastic mean field approach (SMF),<sup>38</sup> which precedes DISH. SMF allows transitions and considers detailed balance every time-step. However, implementing SMF is more complex than DISH. Further study of the DISH properties, implementation of the SMF approach, or incorporation of decoherence into FSSH,<sup>39,40</sup> are needed in order to model both intra- and interband processes with the same NAMD methodology.

We adopt a simulation cell based on a 2x2x2 expansion of cubic MAPbI<sub>3</sub> perovskite. The MA

cations are oriented along the  $\langle 111 \rangle$  direction in the initial structure (Figure 1). The MA cations rotate during heating, equilibration, and NA-MD.<sup>41,42</sup> The cubic structure enables us to investigate the effect of MA rotation in a systematic manner, by considering fewer atomic motions and minimizing the number of non-equivalent degrees of freedom, compared to other perovskite structures.<sup>42</sup> Geometry optimization, electronic structure calculation, and adiabatic MD are carried out using Vienna Ab initio Simulation Package.<sup>43</sup> The generalized gradient approximation of Perdew–Burke–Ernzerho<sup>44</sup> is used to treat the exchange–correlation interactions. The projector-augmented wave approach is used to describe the electron-ion interactions, allowing efficient calculations of the NACs.<sup>45,46</sup> The plane-wave energy cutoff of 400 eV and the 3x3x3 Monkhorst-Pack k-point mesh are adopted for geometry optimization and MD. The van der Waals interactions are accounted for by the Grimme DFT-D3 method.<sup>47</sup> *Ab initio* MD simulations are utilized to assess the structural dynamics at 100K and 300K. Starting with the same ground-state structure optimized at 0K, repeated velocity rescaling is used to heat the initial frozen configuration to the target temperatures. Upon the heating, 3 ps adiabatic MD simulations are carried out in the canonical ensemble (NVT) with a 1 fs timestep to produce the nuclear trajectories used for calculations of the NA electron-phonon coupling and adiabatic state energies. Calculation of elemental-projected anharmonic score is carried out using the FHI-vibes code.<sup>48</sup>

Relativistic effects leading to strong spin-orbit coupling (SOC) are significant in  $\text{CH}_3\text{NH}_3\text{PbI}_3$  and other lead halide perovskite due to the presence of the heavy lead element. Inclusion of SOC lowers the  $\text{MAPbI}_3$  bandgap by nearly 1 eV.<sup>49</sup> Fortunately, the PBE functional produces the correct bandgap, because of the cancellation of the error induced by neglect of SOC, and the self-interaction error of pure DFT functionals. In order to obtain the correct bandgap including SOC, the use of hybrid DFT functionals or the GW theory is required.<sup>50</sup> Unfortunately, both hybrid functionals and the GW theory

are computationally expensive. Inclusion of SOC adds computational expense as well. Repeatedly performing thousands of electronic structure calculations required for the NAMD simulation becomes prohibitive. Therefore, all the calculations in this work are performed with the PBE functional, which provides the best balance between computational efficiency and accuracies for modelling the electron and phonon dynamics, as well as the couplings between the two in MAPbI<sub>3</sub>.

### 3. Results and Discussion

Hybrid perovskites are mechanically soft and exhibit complex structural dynamics at finite temperatures, involving considerable ionic displacements and molecular rotations. Atomic dynamics of hybrid perovskites has strong influence on their optoelectronic properties. We start by considering thermal fluctuations of lattice atoms. Figure 2 shows 3000 superimposed MD snapshots of MAPbI<sub>3</sub> sampled at 100K and 300K. All atoms fluctuate around their equilibrium positions during MD, and MA cations fill the interstices of the Pb-I lattice, indicating that the structures are thermally stable. The lighter MA cations undergo much larger fluctuations in their positions compared to the heavier Pb and I atoms. The MA cation is able to rotate freely within the inorganic Pb-I framework at finite temperatures. Rotation of the organic cations is strongly coupled to local deformations of the inorganic sub-lattice in the MAPbI<sub>3</sub> perovskite, as evidenced by the MD snapshots shown in Figures 2a,b. Such a dynamical coupling between the organic and inorganic components depends on the symmetry and size of the organic cation, as well as the temperature. We observe that MA cations become progressively disordered as temperature is increased, whereas the magnitude of structural fluctuations of the Pb-I sub-lattice is reduced at the higher temperature. In order to better understand the origin behind this observation, we calculated the averaged nuclear positions along the MD trajectory (Figures

2c,d). The averaged  $[\text{PbI}_6^{4-}]$  octahedra are more tilted at the lower temperature. The statistical analysis of the Pb-I-Pb angles confirms this finding (Figure 2e). The MA cations are more disordered as temperature increases. The volume of the inorganic cage is reduced owing to the considerable thermal motion of MA, resulting in smaller distortions of the Pb-I sub-lattice (deviations of the I-Pb-I bond angle) and suppressed displacement of Pb and I atom in each  $[\text{PbI}_6^{4-}]$  octahedron.

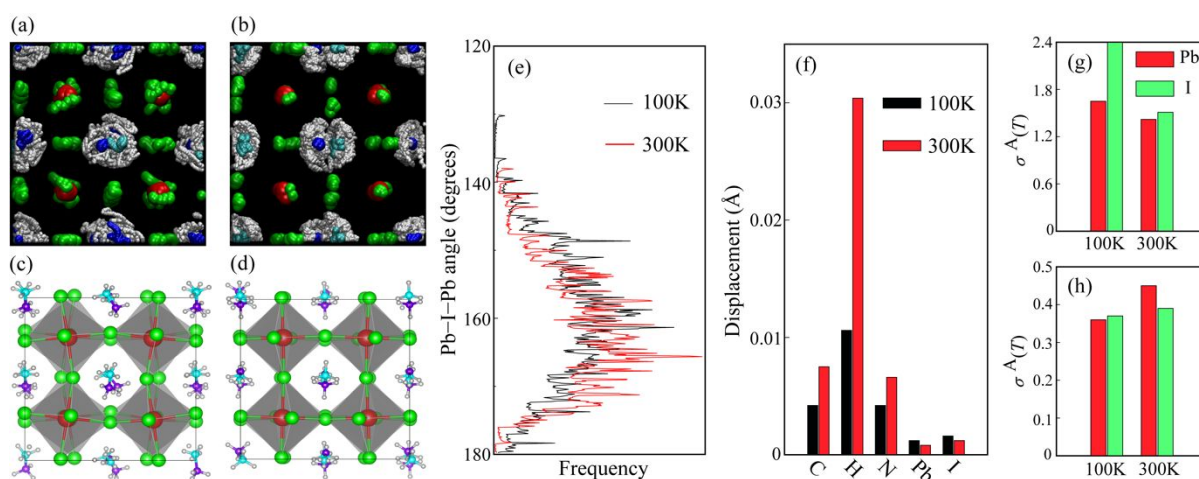


**Figure 2.** 3000 superimposed snapshots from molecular dynamics (MD) trajectories of  $\text{MAPbI}_3$  at 100K (a) and 300K (b).  $\text{MAPbI}_3$  structures averaged over 3000 snapshots of the MD simulation at 100K (c) and 300K (d). Distribution of Pb-I-Pb angles during MD at 100K and 300K (e). Root-mean-square (RMS) displacement for each atom type at the two temperatures (f). Surprisingly, fluctuations of Pb and I decrease at the higher temperature, indicating that the  $[\text{PbI}_6^{4-}]$  octahedra exhibit stronger residual tilting at the lower temperature. Anharmonic score, Eq. (1), of Pb and I atoms in  $\text{MAPbI}_3$  with free (g) and fixed (h) MA cations. Rotation of MA cations at the higher temperature decreases anharmonicity of the inorganic Pb-I lattice (g). Fixing MA gives the opposite trend (h).

In order to quantify thermal motions of the lattice atoms, we computed the root-mean-square (RMS) displacement of each atomic species and averaged them for each temperature, as shown in

Figure 2f. A larger atomic displacement indicates stronger thermal fluctuations. The data show that MA cations exhibit stronger fluctuation than inorganic  $[\text{PbI}_6^{4-}]$  octahedra, which is consistent with the MD snapshots (Figure 2a,b). Crucially, the higher temperature enhances the amplitude of motions of the C, N, and H atoms, but suppresses vibrations of the inorganic Pb and I atoms. This phenomenon occurs because the increased re-orientational motions of the MA cations in the interstitial regions of the Pb-I sub-lattice induce steric hinderance and restrict fluctuations of the inorganic sublattice. To verify this interpretation, we calculated the atomic displacements in  $\text{MAPbI}_3$  at 300K with the MA cations frozen (Figure S1). The inorganic Pb and I atoms fluctuate much more when the MA cations are immobile. The results provide a clear indication of the strong coupling between local deformations of the inorganic  $[\text{PbI}_6^{4-}]$  octahedra and re-orientations of the MA cations. We note that such structural fluctuation dynamics of  $\text{MAPbI}_3$  has been reported in the previous experimental work,<sup>51</sup> e.g., low temperature favors the strongly deformed  $[\text{PbI}_6^{4-}]$  octahedra which restricts the rotational motion of MA, whereas increasing temperature leads to the larger atomic displacements of MA and less distorted  $[\text{PbI}_6^{4-}]$  octahedra. Interestingly, the RMS displacement of H atoms is increased by a factor of 3 as temperature increases from 100K to 300K, compared to a much smaller increase in the atomic displacements of C and N. This observation correlates with the fact that MA tends to deprotonate under the PSC operational conditions. Recent works demonstrated that H vacancies<sup>52</sup> or interstitials<sup>53</sup> can be present in hybrid perovskites and form nonradiative recombination centers. This fact has been long overlooked in PSCs.

Vibrational anharmonicity is known to be important for the optoelectronic properties of semiconductors.<sup>54–58</sup> The “soft” nature of the perovskite crystal lattice suggests that anharmonic effects may be strong in this class of materials. Considerable efforts have been dedicated to establish the origin

of anharmonicity in hybrid perovskites.<sup>56,59–63</sup> It has been shown that the vibrational anharmonicity in MHPs is associated with the displacement of halogen atoms perpendicular to the Pb-X-Pb bonding axis.<sup>64,65</sup> *Ab initio* MD simulations can naturally account for temperature and anharmonic effects in materials, offering an opportunity to directly explore anharmonicity of atomic vibrations. In order to quantitatively estimate the degree of anharmonicity in the MAPbI<sub>3</sub> perovskite at different temperatures, we calculated the anharmonic score,  $\sigma^A(T)$ , at temperature T according to the following expression:<sup>55</sup>

$$\sigma^A(T) = \frac{\sqrt{\sum_{I,\alpha} \langle (F_{I,\alpha}^A)^2 \rangle_T}}{\sqrt{\sum_{I,\alpha} \langle (F_{I,\alpha}^{(2)})^2 \rangle_T}} \quad (1)$$

in which  $F_{I,\alpha}$  is the force on atom I along the  $\alpha$  Cartesian direction, and  $\langle \cdot \rangle_T$  denotes canonical averaging.  $F_{I,\alpha}^A$  represents the anharmonic force component, calculated as the difference between  $F_{I,\alpha}$  and the harmonic force component,  $F_{I,\alpha}^{(2)}$ . The calculated  $\sigma^A(T)$  associated with the inorganic atoms of MAPbI<sub>3</sub> are shown in Figure 2g. We focus on anharmonicity of the inorganic atoms only, because no reliable reference harmonic model can be used for the MA cations, since they randomly rotate at ambient temperature. The anharmonic scores of the Pb and I atoms are relatively large, within the range of 1.2~2.4, which is about an order of magnitude larger than for other common semiconductors, such as Si,<sup>55</sup> Cu<sub>2</sub>ZnSnS<sub>4</sub>,<sup>58</sup> evidencing that MAPbI<sub>3</sub> is strongly anharmonic. Such significant anharmonic effects have been detected in MHPs previously and correlated with several important optoelectronic properties.<sup>64,66,67</sup>

As temperature increases, the anharmonic scores of the inorganic atoms reduce. Anharmonicity is associated with large-amplitude atomic displacements. The amplitudes of the Pb and I displacements decrease as temperature grows, rationalizing the weaker anharmonicity of the Pb and I atoms at the higher temperature. Interestingly, temperature influences the anharmonicity of I atoms much more significantly than the Pb atoms. This is because the MA cations, which rotate inside the inorganic cage,

interact with the I atoms directly, while influencing the Pb atoms indirectly. We emphasize that the weaker anharmonicity at the higher temperature is linked with the smaller displacement of the I atoms perpendicularly to the nearby Pb-Pb axes, helping to maintain the perfect cubic symmetry at the higher temperature. We also compute the anharmonic score with frozen MA cations, Figure 2h. The anharmonic scores of the Pb and I atoms increase with temperature when MA cations are fixed. Further, the anharmonic scores of the Pb and I atoms with MA fixed are much lower than those in the freely moving system, demonstrating that the degree of vibrational anharmonicity of the inorganic Pb-I lattice is strongly associated with its coupling to the rotational motions of the organic cations. These results carry important implications for the properties of the band edge states, which are derived from orbitals of the Pb and I atoms. In this regard, it is of particular importance to link the anharmonic motions of the lattice atoms of the hybrid perovskite with electron-phonon interactions, as we discuss below.

In Figure 3 we report the atom pair radial distribution function (RDF) for MAPbI<sub>3</sub> obtained from the *ab initio* MD simulation at the different temperatures. The RDF can provide quantitative information about structures on the atomic scale. The peak position directly gives the bond length information. The positions of the main peaks of the simulated RDF agree with experiment<sup>68,69</sup> and available theoretical reports<sup>70-72</sup> on the MAPbI<sub>3</sub> perovskite, indicating that the ion dynamics, average structure, and atomic displacements were correctly described by our simulation. The pair RDFs of MAPbI<sub>3</sub> show little variations with temperature. In particular, the Pb-I RDF shows a peak centered at around 3.2 Å. The peak narrows at the higher temperature, indicating a reduced fluctuation in the Pb-I bond length and a more ordered arrangement the Pb and I atoms associated with smaller tilting of the inorganic [PbI<sub>6</sub><sup>4-</sup>] octahedra. Previous work reported a correlation between Pb-I bond fluctuations and stability of the perovskite system.<sup>73</sup> In this regard, our data further confirm that the cubic phase of the

MAPbI<sub>3</sub> perovskite is a high-temperature stable phase, as well-known experimentally. Figure 3b reports the H-I RDF at different temperatures to illustrate possible hydrogen-bonding interactions in MAPbI<sub>3</sub>.<sup>74,75</sup> The H-I RDF shows two maxima at about 3.9 Å and 3.7 Å, which can be ascribed to the different H-I coordination. The two peaks change little with temperature. However, subtle difference can still be found. The H-I RDF peak intensity is slightly smaller at 300K than 100K, suggesting weakened NH⋯I interactions. This is because MA cations rotate more at the higher temperature,<sup>76</sup> reducing hydrogen bonding contacts. In contrast, at the lower temperature, MA cations are partially ordered by hydrogen bonding to iodines, causing tilting of the inorganic [PbI<sub>6</sub><sup>4-</sup>] octahedra.

In order to investigate how anharmonicity influences vibrational properties of the perovskite system, we calculated the vibrational density of states (VDOS) through Fourier transform of the velocity-velocity autocorrelation function obtained from *ab initio* MD:

$$VDOS(\omega) = \frac{1}{N_{ion}} \sum_i^{N_{ion}} \int_0^\infty \langle v_i(\tau) v_i(0) \rangle e^{i\omega\tau} d\tau \quad (2)$$

Here,  $v_i(\tau)$  represents the velocity of atom  $i$  at time  $t$ , and  $\langle \dots \rangle$  denotes ensemble averaging. This methodology is suitable for describing VDOS beyond the harmonic approximation at 0K, characterizing temperature dependent vibrational properties. Figure 3e,f presents the MAPbI<sub>3</sub> VDOS calculated at the different temperatures. The phonon modes in the VDOS spectra can be separated into three regimes. The lowest-frequency regime is below 150 cm<sup>-1</sup>, the middle-frequency regime ranges from 280 to 1700 cm<sup>-1</sup>, and the highest-frequency regime is beyond 2900 cm<sup>-1</sup>, agreeing with the experimentally and theoretically reported vibrational densities of states.<sup>77</sup> The low-frequency phonon modes are completely associated with motion of Pb and I atoms.<sup>78</sup> The phonon modes in the middle-frequency region mostly correspond to the stretching and torsion modes of MA involving relative movement of the -CH<sub>3</sub> and -NH<sub>3</sub> groups. A large phonon frequency gap is present between the low-

and middle-frequency regions, reducing cross-gap phonon scattering between internal motions of the MA cation and vibrations of the inorganic  $[\text{PbI}_6^{4-}]$  octahedrons.<sup>79</sup> The highest-frequency phonon modes mainly correspond to stretching of C-H and N-H bonds. Motion of H atoms dominates this frequency region. We find that higher temperature weakens the low-frequency phonons, enhances the middle-frequency phonons, and suppresses the high-frequency phonons, suggesting that the enhanced MA motion can “lock” fluctuations of inorganic lead and iodine atoms, and further decrease possible formation of the hydrogen bonding. These results provide solid evidence that rotation of MA cations is dynamically coupled to the fluctuations of the inorganic cage.

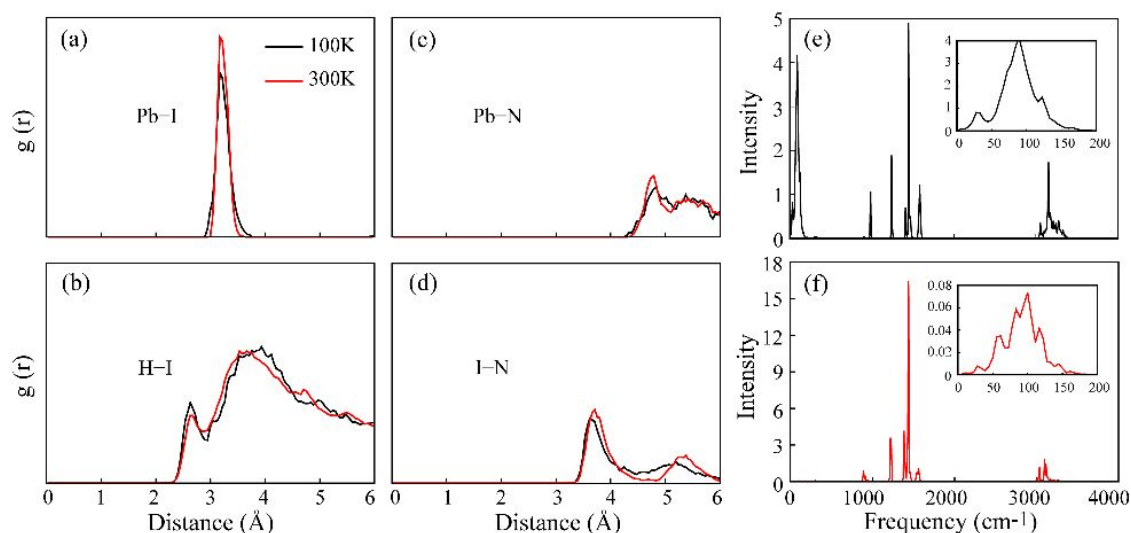


**Figure 3.** Radial distribution functions (RDFs) for the Pb–I, H–I, Pb–N, and I–N atom pairs in  $\text{MAPbI}_3$  (a,b,c,d). The Pb–I RDF shows a higher and sharper peak at the higher T, indicative of changes in the  $[\text{PbI}_6^{4-}]$  internal bonding and octahedra tilting. The Pb–N and I–N RDFs become sharper as well. The H–I RDF changes little. Fourier transform (FT) of the velocity autocorrelation functions averaged over all atoms at 100K (e) and 300K (f). The overall FT intensity increases at the higher temperature; however, the intensity of the low frequency, sub-200  $\text{cm}^{-1}$  peaks decreases, indicating that the  $[\text{PbI}_6^{4-}]$  lattice moves less at the higher temperature.

Next, we consider the effects of thermal fluctuations on the electronic density of states (DOS) around the band edges for the MAPbI<sub>3</sub> perovskite. The thermally averaged DOS at 100K and 300K are shown in Figure 4 along with the DOS of the static structure. The averaging is performed over 100 snapshots randomly sampled from the *ab initio* MD trajectories. The overall DOS shape changes little upon temperature increase. The DOS for the static structure shows a bandgap of 1.63 eV, at the PBE level of theory, which is in agreement with the experimental value.<sup>80</sup> The agreement between theory and experiment with bare DFT functional can be attributed to a fortuitous cancelation of the self-interaction error and neglect of spin-orbit coupling. Thermally averaged electronic bandgap is slightly larger than the static electronic bandgap at 0K. This is in line with the experiments showing blue-shift in the bandgap upon warming of the MAPbI<sub>3</sub> perovskite.<sup>81,82</sup> Two factors contribute to the blue-shift.<sup>83</sup> The valence band maximum (VBM), originates from antibonding interaction of I-*p* and Pb-*s* orbitals, while the conduction band maximum (CBM) originates primarily from non-bonding Pb-*p* orbitals. The antibonding overlap of I-*p* and Pb-*s* orbitals is largest in the perfectly cubic structure. The large overlap upshifts the VBM, and thus, reduces the bandgap. However, the Pb-I bond length increases at the higher temperature, which favors weaker antibonding coupling, and therefore, an increased bandgap. In the present calculations, changes in the Pb-I bond length dominate changes in the Pb-I-Pb bond angle, leading to an increased bandgap at the increased temperature. MA cations contribute little to the DOS around the bandgap. However, they influence the band edge states indirectly through interaction with the Pb-I network causing distortions of the inorganic [PbI<sub>6</sub><sup>4-</sup>] octahedra, complementing the viewpoint that the only role of the organic cation is to electrostatically stabilize the perovskite structure.<sup>84</sup> The main difference of the DOS plots between 100K and 300K is the decreased DOS (orbital level) fluctuations at the higher temperature, a consequence of the weakened anharmonic

effects associated with reduced amplitudes of Pb and I motions. Typically, smaller orbital level fluctuations correspond to weaker electron-phonon coupling, and in particular, to smaller NAC values, since NACs depend on changes in wave functions induced by nuclear motions.

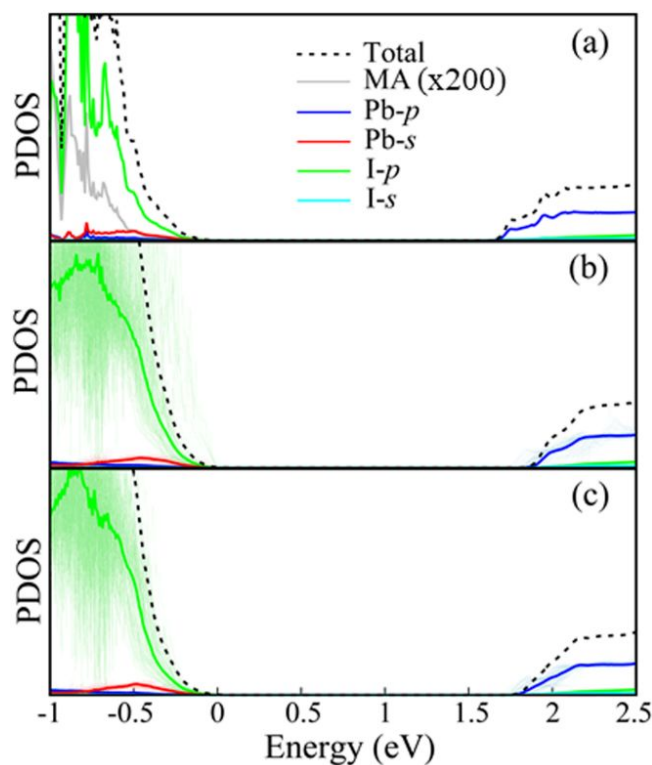


**Figure 4.** Total and projected density of states (PDOS) of MAPbI<sub>3</sub> for the optimized ground-state structure at 0K (a). PDOS fluctuations (thin lines) and averaged PDOS (thick lines) obtained using 100 random MD structures at 100K (b) and 300K (c). PDOS of lighter iodines shows much larger fluctuation than PDOS of heavier Pb. PDOS fluctuates less at the higher temperature owing to the suppressed motion of Pb and I atoms, Figure 2.

Next, we compare the NACs at 100K and 300K. Figure 5a,b shows a 2D map representation of NAC absolute values for all pairs of orbitals in the energy range considered, which are further averaged over the 3 ps MD trajectories. For both systems, the NAC along the sub-diagonal lines is strong, indicating that nonradiative transitions are more likely to happen between nearby states with similar

energies. Smaller NACs are obtained between the states separated by large gaps. This is because the NAC strength is inversely proportional to the energy gap. Nevertheless, quantum transitions between distant states are possible owing to non-zero NACs. The NACs between VB states are significantly larger than between CB states, and therefore, one may expect faster relaxation of holes than electrons. The difference can be ascribed to the larger VB DOS, and correspondingly, smaller energy spacings between VB levels. Smaller NAC is observed between states close to the VBM or CBM, as evidenced by the lighter color near band edges, because the DOS decreases near the band edges. Generally, elevated temperature increases the NAC between states inside the VB and CB. This is likely contributed by the enhanced MA motion at higher temperature, since MA contributes, though very slightly, to deep VB and CB states (see the magnified contribution of the MA cation to the DOS in Figure 4a). Figure 5e,f presents the probability density distribution of NAC magnitudes for all pairs of states along the MD trajectories. Most of the NAC values are less than 1 meV, with a smaller probability of larger NACs in the range of 2-4 meV. The distribution shifts slightly to the larger value at the higher temperature. The NAC that couples the VBM and the CBM decreases at the higher temperature, in contrast to the average behavior of NAC for transitions inside the bands. The decrease can be attributed to the smaller displacements and decreased anharmonicity of the Pb and I atoms, Figure 2. The band edge states are localized exclusively on the atoms of the inorganic lattice, and the reduced motions of these atoms are responsible for the smaller NAC. The changes in the NAC at different temperatures should induce modifications in both intra-band charge relaxation and electron-hole recombination across the bandgap.

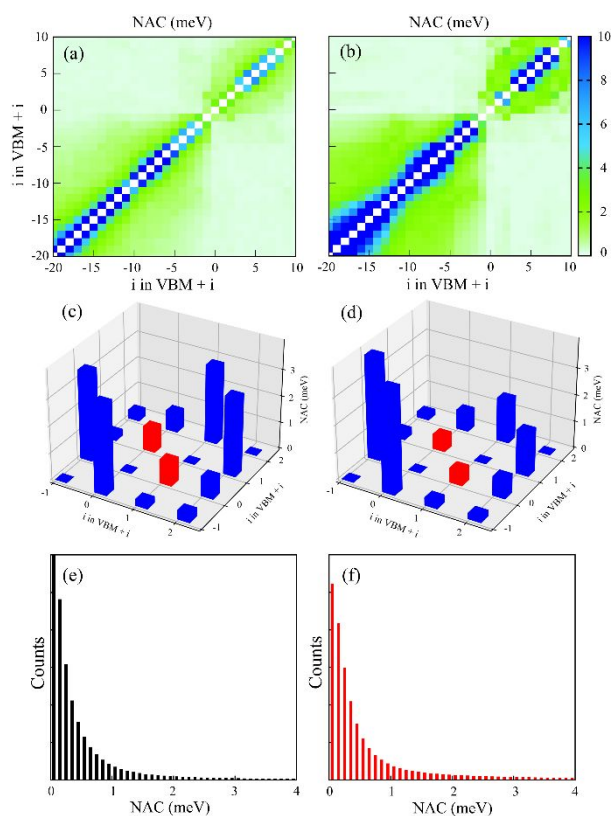


**Figure 5.** Thermally averaged absolute nonadiabatic couplings (NAC) **(a,b,c,d)** and their distributions **(e, f)** for all pairs of states sampled over the MD trajectories at 100K **(a,c,e)** and 300K **(b,d,f)**. Parts **(c,d)** focus the region near the band edges, with the red bar denoting the VBM-CBM NAC. VB states are coupled to each other more strongly than CB states because the VB DOS is higher than the CB DOS, Figure 4. Higher temperature generally enhances NAC between states inside VB and CB; however, the VBM-CBM NAC is weaker at the higher temperature. The NAC distribution is shifted slightly toward larger values above 2 meV at the higher temperature, **(f)** vs **(e)**.

Finally, we investigate the carrier relaxation processes, as defined in Figure 1, using the state-of-the-art theoretical methodologies developed in our group. The data for the electron/hole cooling and electron-hole recombination processes are shown in Figure 6a,b and 6c,d, respectively. To facilitate the comparison, the initial states of the carrier cooling processes correspond to an energy of ca. 0.5 eV

below or above the VBM or the CBM. The simulated hot carrier cooling times are a few hundreds of femtoseconds, falling within the range reported experimentally. Hot holes relax faster than that electron, while elevated temperature accelerates both electron and hole relaxations (Figure 6a,b). The reported timescales are obtained by exponential fitting of the NA-MD simulation data. The cooling time decreases from 614.9 fs to 284.8 fs for electrons and from 313.4 fs to 105.2 fs for holes between 100K and 300K, in agreement with the transient absorption spectroscopy characterization of temperature-dependent carrier intraband relaxation by Diroll.<sup>18</sup> This can be explained by the stronger NAC within the VB and CB state manifolds at the higher temperature (Figure 5). The temperature-induced acceleration of carrier cooling observed in hybrid perovskites follows the same trend as electron-vibrational relaxation in most metals and semiconductors, which show faster intraband relaxation with increasing temperature.<sup>18</sup> The simulated timescale of nonradiative electron-hole recombination is several nanoseconds (Figure 6c), which is also in agreement with experiment.<sup>2</sup> In contrast to the intraband carrier relaxation, the electron-hole recombination slows down by a factor of ca. 2 at the higher temperature, which can be ascribed to the smaller NAC between the VBM and the CBM (Figure 5c,d) and a slightly larger bandgap (Figure 4c). The elastic electron-vibrational scattering, characterized by the pure-dephasing time (Figure 6d) is also slower at 300K (Figure 6d). Such anomalous temperature-dependence of the nonradiative charge recombination is also consistent with experiment.<sup>13</sup> The slower charge recombination observed at the higher temperature is particularly important for PSC performance, because solar cells heat up under sunlight, and longer charge carrier lifetime is critical for approaching the Shockley-Quisser efficiency limit.

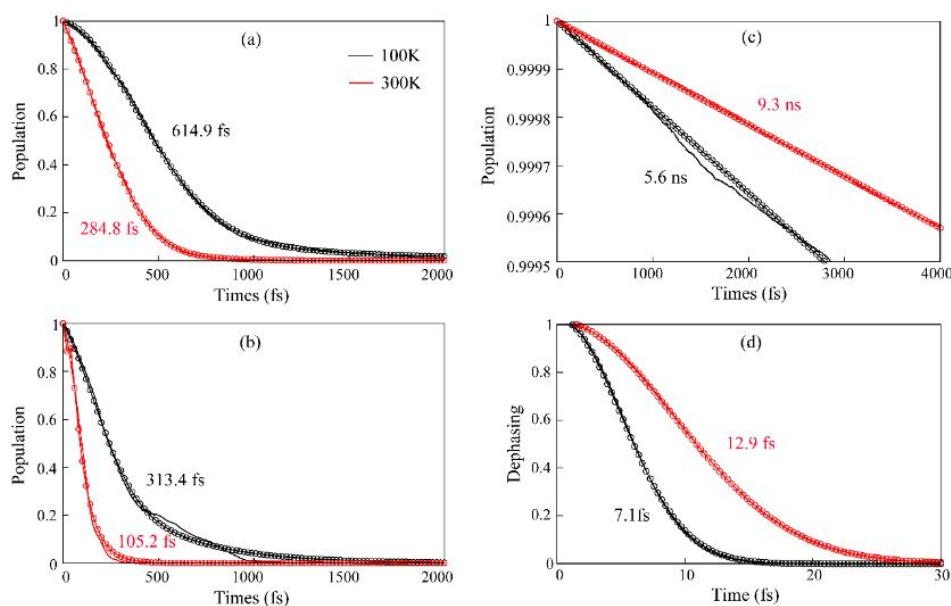


**Figure 6.** Evolution of excited state populations of hot electrons **(a)** and holes **(b)** with the excess energy of ca. 0.5 eV. Higher temperature accelerates both electron and hole relaxation. Nonradiative electron-hole recombination **(c)**. The recombination takes nanoseconds and is slower at the higher temperature due to the smaller nonadiabatic coupling, Figure 5c,d. Pure-dephasing functions for the lowest-energy electronic excitation **(d)**. Pure-dephasing characterizes elastic electron-phonon scattering. The inverse of the pure-dephasing time gives the homogeneous single-particle optical linewidth. Both inelastic (relaxation) and elastic (pure-dephasing) electron-phonon scattering involved in the electron-hole recombination, parts (c) and (d), are slowed down at the higher temperature, due to reduced motions of the Pb-I lattice, Figure 2.

Nonradiative relaxation across large energy gaps in the current and other systems occurs by NA transitions, rather than by an adiabatic thermally activated barrier crossing, because the geometry distortion needed for the initial and final electronic levels to cross requires a very large amount of energy and is highly unlikely. For this reason, if a rate formula is needed, the Fermi golden rule is more appropriate than a Marcus theory expression for a thermally activated process.<sup>85</sup> The NA

transition rate is temperature dependent because the NAC involves atomic velocity, which changes with temperature, and because the Franck-Condon factor, whose time-domain analog is decoherence,<sup>86</sup> evaluated in the present calculations, also depends on temperature. Since crossing of the initial and final electronic energy levels for the nonradiative charge recombination across the bandgap is very unlikely, NA transitions happen away from the crossings. The NAC for transitions across large gaps is small, since it is inversely proportional to the energy gap. For this reason, the electron-hole recombination across the bandgap requires nanoseconds and is much slower than the sub-picosecond intraband charge relaxation. In comparison, a Marcus theory estimate for the rate of a thermally activated electron-hole recombination across the bandgap would produce a very small number, on the order of  $10^{-50}\text{s}^{-1}$ .

Multiple arguments have been put forth in order to rationalize the long carrier lifetimes in MHPs. In addition to the effects discussed here, other microscopic mechanisms include formation of polarons and ferroelectric domains, and the Rashba effect have been proposed. Polaron formation and ferroelectric domains are related to orientation of the organic cations and structural distortions of the inorganic lattice. Ferroelectric domains arising from stable and relatively large-scale distortions of the system structure help separating the electrons and holes, thus decreasing their interaction.<sup>87</sup> Formation of polarons, by rotation of the organic cations and structural distortion of the lattice, screens photo-generated or injected charges, also reducing their interaction.<sup>88</sup> The Rashba effect can cause the lowest energy excited state to attain a significant triplet character, decoupling it from the singlet ground state, and slowing down the excited-to-ground state decay.<sup>89</sup> The effects discussed in the present work are distinct from these mechanisms in general. One can draw an analogy between the enhanced rotation of the organic cations that assists in formation of large polarons and charge screening, and the enhanced

rotation of the organic cations that suppresses motions of the inorganic lattice, both phenomena extending the charge carrier lifetimes. Ferroelectric domains are ruled out in the current case because their formation requires alignment of the organic MA cations, and they are known to rotate relatively freely in MAPbI<sub>3</sub> at ambient temperatures.<sup>90</sup>

Point defects are abundant in MHPs and often introduce states inside the bandgap, as well as states inside the VB and CB. Because MHPs are soft, compared to the traditional inorganic semiconductors, such as Si or CdSe, thermal fluctuations can have a strong influence on defect energy levels.<sup>91–93</sup> Mid-gap defects, which are considered to be shallow based on electronic structure calculation performed on the optimized crystal geometry, can be changed into deep states by thermally induced atomic fluctuation. Conversely, deep defects, as judged on the basis of the electronic structure at 0K, can become shallow because of the thermal fluctuation.<sup>91–93</sup> Such dynamic behavior becomes more pronounced as temperature increases. The thermal influence on defect energy levels has several important implications for the charge carrier dynamics and light harvesting. Fluctuation of defect levels between shallow and deep states both accelerates charge trapping, and allows charges to escape back into bands, if defect energy levels approach band edges within several  $k_B T$ . Such defect behavior is distinct from the Shockley–Read–Hall (SRH) interpretation of defect levels in the traditional semiconductors.<sup>94</sup> In the SRH description, defect state energies are assumed to fluctuate little at a finite temperature, and trapped charges cannot escape back into bands. Defects that act as strong charge recombination centers in the SRH model may be less detrimental in the softer halide perovskites. A defect level fluctuating over a broad energy range can extend light absorption into the red region of the solar spectrum, improving light harvesting.

#### 4. Conclusion

We have studied the nonradiative relaxation dynamics of charge carriers of the  $\text{MAPbI}_3$  perovskite using NA-MD simulations combined with time-domain DFT. The simulations show that an elevated temperature enhances the rotation of the MA cations, leading to a large steric hindrance that suppresses fluctuations of the Pb-I lattice. We quantified the anharmonicity of  $\text{MAPbI}_3$ , and found that the anharmonic effect is strong in this class of materials, as compared to the traditional semiconductors. The anharmonicity can be attributed to both the softness of the material, and coupling of rotations of the organic cations with fluctuations of the inorganic lattice. The latter factor is further supported by the decreased anharmonic score of the inorganic atoms when the MA cations are artificially frozen in the simulations. Furthermore, the anharmonicity of both Pb and I atoms weakens with the increasing temperature. This can be attributed to the overall reduced amplitudes of motions of the Pb and I atoms at higher temperature that are hindered by the fast cation rotations. The hydrogen-bonding interactions between the MA cations and the iodines in the lattice are weakened at higher temperature, since the MA cations rotate more and are dynamically disordered. The observed orientation motion of the MA cation and fluctuations of Pb-I lattice at varying temperatures is related to the excellent photovoltaic performance of hybrid perovskites. We demonstrated that the  $\text{MAPbI}_3$  perovskite exhibits opposite temperature dependence of hot electron and hole relaxation, and electron-hole recombination. Elevated temperature increases the carrier cooling rate, but slows the nonradiative charge recombination across the bandgap, in agreement with experiment. The latter result is important for reaching good solar cells performance, since solar cells can be heated up by the solar radiation during their operation. Such peculiar behavior is rationalized by the opposite trends in the temperature dependence of the NACs responsible for intraband charge relaxation and interband charge recombination, stemming from the

different dependence of fluctuations of the organic and inorganic components on temperature. The detailed atomistic insights into the temperature-dependent charge carrier relaxation in the MAPbI<sub>3</sub> perovskite, originating from the complex interplay between rotations of the organic cations and fluctuations of the inorganic Pb-I lattice, provide valuable guidelines for further optimization of the photovoltaic response of PSCs. In particular, the increased charge carrier lifetimes at higher temperatures is rather unique to hybrid organic-inorganic perovskites, allowing them to maintain excellent performance even when heated under operating conditions. Atomistic understanding the mechanism underlying this important property guides design and discovery of other efficient and inexpensive materials for optoelectronic and solar energy devices.

**Acknowledgements.** We are grateful to Dr. Florian Knoop for fruitful discussions. W.L. acknowledges financial support of the National Natural Science Foundation of China (No. 21903023), Science and Technology Innovation Program of Hunan Province (No. 2021RC3089), and China Postdoctoral Science Foundation (2021M701168). J.Y. acknowledge financial support from the UNSW Materials and Manufacturing Futures Institute. O.V.P. acknowledges financial support of the U.S. Department of Energy (DE-SC0014429).

**Supporting Information.** Displacements of Pb and I atoms with free and frozen MA cations.

## References

- (1) Cherniukh, I.; Rainò, G.; Stöferle, T.; Burian, M.; Travesset, A.; Naumenko, D.; Amenitsch, H.; Erni, R.; Mahrt, R. F.; Bodnarchuk, M. I.; Kovalenko, M. V. Perovskite-Type Superlattices from Lead Halide

- Perovskite Nanocubes. *Nature* **2021**, *593* (7860), 535–542. <https://doi.org/10.1038/s41586-021-03492-5>.
- (2) Xing, G.; Mathews, N.; Sun, S.; Lim, S. S.; Lam, Y. M.; Gratzel, M.; Mhaisalkar, S.; Sum, T. C. Long-Range Balanced Electron- and Hole-Transport Lengths in Organic-Inorganic CH<sub>3</sub>NH<sub>3</sub>PbI<sub>3</sub>. *Science* **2013**, *342* (6156), 344–347. <https://doi.org/10.1126/science.1243167>.
- (3) Duan, B.; Ren, Y.; Xu, Y.; Chen, W.; Ye, Q.; Huang, Y.; Zhu, J.; Dai, S. Identification and Characterization of a New Intermediate to Obtain High Quality Perovskite Films with Hydrogen Halides as Additives. *Inorg. Chem. Front.* **2017**, *4* (3), 473–480. <https://doi.org/10.1039/C6QI00492J>.
- (4) Boziki, A.; Kubicki, D. J.; Mishra, A.; Meloni, S.; Emsley, L.; Grätzel, M.; Rothlisberger, U. Atomistic Origins of the Limited Phase Stability of Cs<sup>+</sup>-Rich FA<sub>x</sub>Cs<sub>(1-x)</sub>PbI<sub>3</sub> Mixtures. *Chem. Mater.* **2020**, *32* (6), 2605–2614. <https://doi.org/10.1021/acs.chemmater.0c00120>.
- (5) Jian, W.; Jia, R.; Zhang, H.-X.; Bai, F.-Q. Arranging Strategies for A-Site Cations: Impact on the Stability and Carrier Migration of Hybrid Perovskite Materials. *Inorg. Chem. Front.* **2020**, *7* (8), 1741–1749. <https://doi.org/10.1039/D0QI00102C>.
- (6) Yin, J.; Li, H.; Cortecchia, D.; Soci, C.; Brédas, J.-L. Excitonic and Polaronic Properties of 2D Hybrid Organic–Inorganic Perovskites. *ACS Energy Lett.* **2017**, *2* (2), 417–423. <https://doi.org/10.1021/acsenergylett.6b00659>.
- (7) Biswas, A.; Bakthavatsalam, R.; Kundu, J. Efficient Exciton to Dopant Energy Transfer in Mn<sup>2+</sup>-Doped (C<sub>4</sub>H<sub>9</sub>NH<sub>3</sub>)<sub>2</sub>PbBr<sub>4</sub> Two-Dimensional (2D) Layered Perovskites. *Chem. Mater.* **2017**, *29* (18), 7816–7825. <https://doi.org/10.1021/acs.chemmater.7b02429>.
- (8) *Best Research Cell Efficiency (National Renewable Energy Laboratory)*. <https://www.nrel.gov/pv/assets/pdfs/best-research-cell-efficiencies.20190802.pdf> (accessed 2021-10-01).
- (9) Jung, H. S.; Park, N.-G. Perovskite Solar Cells: From Materials to Devices. *Small* **2015**, *11* (1), 10–25.

<https://doi.org/10.1002/sml.201402767>.

- (10) Madjet, M. E.; Berdiyrov, G. R.; El-Mellouhi, F.; Alharbi, F. H.; Akimov, A. V.; Kais, S. Cation Effect on Hot Carrier Cooling in Halide Perovskite Materials. *J. Phys. Chem. Lett.* **2017**, *8* (18), 4439–4445. <https://doi.org/10.1021/acs.jpcllett.7b01732>.
- (11) Ghosh, D.; Acharya, D.; Pedesseau, L.; Katan, C.; Even, J.; Tretiak, S.; Neukirch, A. J. Charge Carrier Dynamics in Two-Dimensional Hybrid Perovskites: Dion–Jacobson vs. Ruddlesden–Popper Phases. *J. Mater. Chem. A* **2020**, *8* (42), 22009–22022. <https://doi.org/10.1039/D0TA07205B>.
- (12) Herz, L. M. Charge-Carrier Dynamics in Organic-Inorganic Metal Halide Perovskites. *Annu. Rev. Phys. Chem.* **2016**, *67*(1), 65–89. <https://doi.org/10.1146/annurev-physchem-040215-112222>.
- (13) Milot, R. L.; Eperon, G. E.; Snaith, H. J.; Johnston, M. B.; Herz, L. M. Temperature-Dependent Charge-Carrier Dynamics in CH<sub>3</sub>NH<sub>3</sub>PbI<sub>3</sub> Perovskite Thin Films. *Adv. Funct. Mater.* **2015**, *25* (39), 6218–6227. <https://doi.org/10.1002/adfm.201502340>.
- (14) Long, R.; Liu, J.; Prezhdov, O. V. Unravelling the Effects of Grain Boundary and Chemical Doping on Electron–Hole Recombination in CH<sub>3</sub>NH<sub>3</sub>PbI<sub>3</sub> Perovskite by Time-Domain Atomistic Simulation. *J. Am. Chem. Soc.* **2016**, *138* (11), 3884–3890. <https://doi.org/10.1021/jacs.6b00645>.
- (15) Peng, J.; Chen, Y.; Zheng, K.; Pullerits, T.; Liang, Z. Insights into Charge Carrier Dynamics in Organo-Metal Halide Perovskites: From Neat Films to Solar Cells. *Chem. Soc. Rev.* **2017**, *46* (19), 5714–5729. <https://doi.org/10.1039/C6CS00942E>.
- (16) Li, Z.; Chen, Y.; Burda, C. Photoexcited Dynamics in Metal Halide Perovskites: From Relaxation Mechanisms to Applications. *J. Phys. Chem. C* **2019**, *123* (6), 3255–3269. <https://doi.org/10.1021/acs.jpcc.8b11347>.
- (17) Kahmann, S.; A. Loi, M. Hot Carrier Solar Cells and the Potential of Perovskites for Breaking the Shockley–

- Queisser Limit. *J. Mater. Chem. C* **2019**, *7*(9), 2471–2486. <https://doi.org/10.1039/C8TC04641G>.
- (18) Diroll, B. T. Temperature-Dependent Intraband Relaxation of Hybrid Perovskites. *J. Phys. Chem. Lett.* **2019**, *10*(18), 5623–5628. <https://doi.org/10.1021/acs.jpcclett.9b02320>.
- (19) Rosenwaks, Y.; Hanna, M. C.; Levi, D. H.; Szmyd, D. M.; Ahrenkiel, R. K.; Nozik, A. J. Hot-Carrier Cooling in GaAs: Quantum Wells versus Bulk. *Phys. Rev. B* **1993**, *48* (19), 14675–14678. <https://doi.org/10.1103/PhysRevB.48.14675>.
- (20) Lee, J.-W.; Seo, S.; Nandi, P.; Jung, H. S.; Park, N.-G.; Shin, H. Dynamic Structural Property of Organic-Inorganic Metal Halide Perovskite. *iScience* **2021**, *24*(1), 101959. <https://doi.org/10.1016/j.isci.2020.101959>.
- (21) Tully, J. C. Nonadiabatic Molecular Dynamics. *Int. J. Quantum Chem.* **1991**, *40* (S25), 299–309. <https://doi.org/10.1002/qua.560400830>.
- (22) Jaeger, H. M.; Fischer, S.; Prezhdo, O. V. Decoherence-Induced Surface Hopping. *J. Chem. Phys.* **2012**, *137* (22), 22A545. <https://doi.org/10.1063/1.4757100>.
- (23) Akimov, A. V.; Prezhdo, O. V. The PYXAID Program for Non-Adiabatic Molecular Dynamics in Condensed Matter Systems. *J Chem Theory Comput* **2013**, *14*.
- (24) Akimov, A. V.; Prezhdo, O. V. Advanced Capabilities of the PYXAID Program: Integration Schemes, Decoherence Effects, Multiexcitonic States, and Field-Matter Interaction. *J Chem Theory Comput* **2014**, *16*.
- (25) Chen, L.; Tan, T.; Prezhdo, O. V.; Ruan, X. Shape and Temperature Dependence of Hot Carrier Relaxation Dynamics in Spherical and Elongated CdSe Quantum Dots. *J. Phys. Chem. C* **2011**, *7*.
- (26) Madjet, M. E.-A.; Akimov, A. V.; El-Mellouhi, F.; Berdiyrov, G. R.; Ashhab, S.; Tabet, N.; Kais, S. Enhancing the Carrier Thermalization Time in Organometallic Perovskites by Halide Mixing. *Phys. Chem. Chem. Phys.* **2016**, *18*(7), 5219–5231. <https://doi.org/10.1039/C5CP06603D>.
- (27) Li, W.; Zhou, L.; Prezhdo, O. V.; Akimov, A. V. Spin–Orbit Interactions Greatly Accelerate Nonradiative

- Dynamics in Lead Halide Perovskites. *ACS Energy Lett.* **2018**, *3* (9), 2159–2166.  
<https://doi.org/10.1021/acseenergylett.8b01226>.
- (28) Zhang, Z.; Long, R.; Tokina, M. V.; Prezhdo, O. V. Interplay between Localized and Free Charge Carriers Can Explain Hot Fluorescence in the  $\text{CH}_3\text{NH}_3\text{PbBr}_3$  Perovskite: Time-Domain Ab Initio Analysis. *J. Am. Chem. Soc.* **2017**, *139*(48), 17327–17333. <https://doi.org/10.1021/jacs.7b06401>.
- (29) Prezhdo, O. V. Modeling Non-Adiabatic Dynamics in Nanoscale and Condensed Matter Systems. *Acc. Chem. Res.* **2021**, *54*(23), 4239–4249. <https://doi.org/10.1021/acs.accounts.1c00525>.
- (30) Qiao, L.; Fang, W.-H.; Long, R.; Prezhdo, Oleg. V. Elimination of Charge Recombination Centers in Metal Halide Perovskites by Strain. *J. Am. Chem. Soc.* **2021**. <https://doi.org/10.1021/jacs.1c04442>.
- (31) Li, W.; She, Y.; Vasenko, A. S.; Prezhdo, O. V. Ab Initio Nonadiabatic Molecular Dynamics of Charge Carriers in Metal Halide Perovskites. *Nanoscale* **2021**, *13*, 10239–10265.  
<https://doi.org/10.1039/D1NR01990B>.
- (32) Cheng, C.; Fang, W.-H.; Long, R.; Prezhdo, O. V. Water Splitting with a Single-Atom Cu/TiO<sub>2</sub> Photocatalyst: Atomistic Origin of High Efficiency and Proposed Enhancement by Spin Selection. *JACS Au* **2021**.  
<https://doi.org/10.1021/jacsau.1c00004>.
- (33) Wang, Z.; Altmann, P.; Gadermaier, C.; Yang, Y.; Li, W.; Ghirardini, L.; Trovatiello, C.; Finazzi, M.; Duò, L.; Celebrano, M.; Long, R.; Akinwande, D.; Prezhdo, O. V.; Cerullo, G.; Dal Conte, S. Phonon-Mediated Interlayer Charge Separation and Recombination in a MoSe<sub>2</sub>/WSe<sub>2</sub> Heterostructure. *Nano Lett.* **2021**.  
<https://doi.org/10.1021/acs.nanolett.0c04955>.
- (34) Stier, W.; Duncan, W. R.; Prezhdo, O. V. Thermally Assisted Sub-10 Fs Electron Transfer in Dye-Sensitized Nanocrystalline TiO<sub>2</sub> Solar Cells. *Adv. Mater.* **2004**, *16* (3), 240–244.  
<https://doi.org/10.1002/adma.200306027>.

- (35) He, J.; Vasenko, A. S.; Long, R.; Prezhdo, O. V. Halide Composition Controls Electron–Hole Recombination in Cesium–Lead Halide Perovskite Quantum Dots: A Time Domain Ab Initio Study. *J. Phys. Chem. Lett.* **2018**, *9*(8), 1872–1879. <https://doi.org/10.1021/acs.jpcclett.8b00446>.
- (36) Zhou, Z.; Liu, J.; Long, R.; Li, L.; Guo, L.; Prezhdo, O. V. Control of Charge Carriers Trapping and Relaxation in Hematite by Oxygen Vacancy Charge: Ab Initio Non-Adiabatic Molecular Dynamics. *J. Am. Chem. Soc.* **2017**, *139*(19), 6707–6717. <https://doi.org/10.1021/jacs.7b02121>.
- (37) Li, L.; Long, R.; Bertolini, T.; Prezhdo, O. V. Sulfur Adatom and Vacancy Accelerate Charge Recombination in MoS<sub>2</sub> but by Different Mechanisms: Time-Domain Ab Initio Analysis. *Nano Lett.* **2017**, *17*(12), 7962–7967. <https://doi.org/10.1021/acs.nanolett.7b04374>.
- (38) Prezhdo, O. V. Mean Field Approximation for the Stochastic Schrödinger Equation. *J. Chem. Phys.* **1999**, *111*(18), 8366–8377. <https://doi.org/10.1063/1.480178>.
- (39) Bittner, E. R.; Rossky, P. J. Quantum Decoherence in Mixed Quantum-classical Systems: Nonadiabatic Processes. *J. Chem. Phys.* **1995**, *103*(18), 8130–8143. <https://doi.org/10.1063/1.470177>.
- (40) Habenicht, B. F.; Prezhdo, O. V. Nonradiative Quenching of Fluorescence in a Semiconducting Carbon Nanotube: A Time-Domain Ab Initio Study. *Phys. Rev. Lett.* **2008**, *100*(19), 197402. <https://doi.org/10.1103/PhysRevLett.100.197402>.
- (41) Li, W.; Zhan, J.; Liu, X.; Tang, J.; Yin, W.-J.; Prezhdo, O. V. Atomistic Mechanism of Passivation of Halide Vacancies in Lead Halide Perovskites by Alkali Ions. *Chem. Mater.* **2021**, *33*(4), 1285–1292. <https://doi.org/10.1021/acs.chemmater.0c04188>.
- (42) Li, W.; Chen, Z.; Tang, J.; Prezhdo, O. V. Anti-Correlation between Band Gap and Carrier Lifetime in Lead Halide Perovskites under Compression Rationalized by Ab Initio Quantum Dynamics. *Chem. Mater.* **2020**, *32*(11), 4707–4715. <https://doi.org/10.1021/acs.chemmater.0c01287>.

- (43) Kresse, G.; Furthmüller, J. Efficient Iterative Schemes for *Ab Initio* Total-Energy Calculations Using a Plane-Wave Basis Set. *Phys. Rev. B* **1996**, *54* (16), 11169–11186. <https://doi.org/10.1103/PhysRevB.54.11169>.
- (44) Perdew, J. P.; Burke, K.; Ernzerhof, M. Generalized Gradient Approximation Made Simple. *Phys. Rev. Lett.* **1996**, *77* (18), 3865–3868. <https://doi.org/10.1103/PhysRevLett.77.3865>.
- (45) Chu, W.; Zheng, Q.; Akimov, A. V.; Zhao, J.; Saidi, W. A.; Prezhdo, O. V. Accurate Computation of Nonadiabatic Coupling with Projector Augmented-Wave Pseudopotentials. *J. Phys. Chem. Lett.* **2020**, 10073–10080. <https://doi.org/10.1021/acs.jpcclett.0c03080>.
- (46) Chu, W.; Prezhdo, O. V. Concentric Approximation for Fast and Accurate Numerical Evaluation of Nonadiabatic Coupling with Projector Augmented-Wave Pseudopotentials. *J. Phys. Chem. Lett.* **2021**, *12* (12), 3082–3089. <https://doi.org/10.1021/acs.jpcclett.0c03853>.
- (47) Grimme, S.; Antony, J.; Ehrlich, S.; Krieg, H. A Consistent and Accurate *Ab Initio* Parametrization of Density Functional Dispersion Correction (DFT-D) for the 94 Elements H-Pu. *J. Chem. Phys.* **2010**, *132* (15), 154104. <https://doi.org/10.1063/1.3382344>.
- (48) Knoop, F.; Purcell, T. A. r; Scheffler, M.; Carbogno, C. FHI-Vibes: \_Ab Initio\_ Vibrational Simulations. *J. Open Source Softw.* **2020**, *5* (56), 2671. <https://doi.org/10.21105/joss.02671>.
- (49) Even, J.; Pedesseau, L.; Jancu, J.-M.; Katan, C. F. and A. in L. I. P. from M. D. S. S. Importance of Spin-Orbit Coupling in Hybrid Organic/Inorganic Perovskites for Photovoltaic Applications. *J. Phys. Chem. Lett.* **2013**, *4* (17), 2999–3005. <https://doi.org/10.1021/jz401532q>.
- (50) Umari, P.; Mosconi, E.; Angelis, F. D. Relativistic GW Calculations on CH<sub>3</sub>NH<sub>3</sub>PbI<sub>3</sub> and CH<sub>3</sub>NH<sub>3</sub>SnI<sub>3</sub> Perovskites for Solar Cell Applications. *Sci. Rep.* **2014**, *4*, 4467. <https://doi.org/10.1038/srep04467>.
- (51) Weller, M. T.; Weber, O. J.; Henry, P. F.; Di Pumpo, A. M.; Hansen, T. C. Complete Structure and Cation Orientation in the Perovskite Photovoltaic Methylammonium Lead Iodide between 100 and 352 K. *Chem.*

- Commun.* **2015**, *51* (20), 4180–4183. <https://doi.org/10.1039/C4CC09944C>.
- (52) Zhang, X.; Shen, J.-X.; Turiansky, M. E.; Van de Walle, C. G. Minimizing Hydrogen Vacancies to Enable Highly Efficient Hybrid Perovskites. *Nat. Mater.* **2021**, *20* (7), 971–976. <https://doi.org/10.1038/s41563-021-00986-5>.
- (53) Liang, Y.; Cui, X.; Li, F.; Stampfl, C.; Huang, J.; Ringer, S. P.; Zheng, R. Hydrogen-Anion-Induced Carrier Recombination in MAPbI<sub>3</sub> Perovskite Solar Cells. *J. Phys. Chem. Lett.* **2021**, *12* (43), 10677–10683. <https://doi.org/10.1021/acs.jpcclett.1c03061>.
- (54) Yang, J. Mapping Temperature-Dependent Energy–Structure–Property Relationships for Solid Solutions of Inorganic Halide Perovskites. *J. Mater. Chem. C* **2020**, *8* (47), 16815–16825. <https://doi.org/10.1039/D0TC04515B>.
- (55) Knoop, F.; Purcell, T. A. R.; Scheffler, M.; Carbogno, C. Anharmonicity Measure for Materials. *Phys. Rev. Mater.* **2020**, *4* (8), 083809. <https://doi.org/10.1103/PhysRevMaterials.4.083809>.
- (56) Munson, K. T.; Swartzfager, J. R.; Asbury, J. B. Lattice Anharmonicity: A Double-Edged Sword for 3D Perovskite-Based Optoelectronics. *ACS Energy Lett.* **2019**, *4* (8), 1888–1897. <https://doi.org/10.1021/acsenergylett.9b01073>.
- (57) Yang, J.; Wang, Y.; Wu, T.; Li, S. Correlating the Composition-Dependent Structural and Electronic Dynamics of Inorganic Mixed Halide Perovskites. *Chem. Mater.* **2020**, *32* (6), 2470–2481. <https://doi.org/10.1021/acs.chemmater.9b04995>.
- (58) Zhang, P.; Hou, Z.; Jiang, L.; Yang, J.; Saidi, W. A.; Prezhdo, O. V.; Li, W. Weak Anharmonicity Rationalizes the Temperature-Driven Acceleration of Nonradiative Dynamics in Cu<sub>2</sub>ZnSnS<sub>4</sub> Photoabsorbers. *ACS Appl. Mater. Interfaces* **2021**, *13* (51), 61365–61373. <https://doi.org/10.1021/acsami.1c21526>.
- (59) Li, W.; Vasenko, A. S.; Tang, J.; Prezhdo, O. V. Anharmonicity Extends Carrier Lifetimes in Lead Halide

- Perovskites at Elevated Temperatures. *J. Phys. Chem. Lett.* **2019**, *10* (20), 6219–6226.  
<https://doi.org/10.1021/acs.jpcllett.9b02553>.
- (60) Maughan, A. E.; Ganose, A. M.; Candia, A. M.; Granger, J. T.; Scanlon, D. O.; Neilson, J. R. Anharmonicity and Octahedral Tilting in Hybrid Vacancy-Ordered Double Perovskites. *Chem. Mater.* **2018**, *30*(2), 472–483.  
<https://doi.org/10.1021/acs.chemmater.7b04516>.
- (61) Gehrman, C.; Egger, D. A. Dynamic Shortening of Disorder Potentials in Anharmonic Halide Perovskites. *Nat. Commun.* **2019**, *10*(1), 3141. <https://doi.org/10.1038/s41467-019-11087-y>.
- (62) Lanigan-Atkins, T.; He, X.; Krogstad, M. J.; Pajeroski, D. M.; Abernathy, D. L.; Xu, G. N. M. N.; Xu, Z.; Chung, D.-Y.; Kanatzidis, M. G.; Rosenkranz, S.; Osborn, R.; Delaire, O. Two-Dimensional Overdamped Fluctuations of the Soft Perovskite Lattice in CsPbBr<sub>3</sub>. *Nat. Mater.* **2021**, *20* (7), 977–983.  
<https://doi.org/10.1038/s41563-021-00947-y>.
- (63) Guo, Z.; Wang, J.; Yin, W.-J. Atomistic Origin of Lattice Softness and Its Impact on Structural and Carrier Dynamics in Three Dimensional Perovskites. *Energy Environ. Sci.* **2021**.  
<https://doi.org/10.1039/D1EE02131A>.
- (64) Gehrman, C.; Caicedo-Dávila, S.; Zhu, X.; Egger, D. A. Transversal Halide Motion Intensifies Band-To-Band Transitions in Halide Perovskites. *Adv. Sci.* **2022**, *9* (16), 2200706.  
<https://doi.org/10.1002/advs.202200706>.
- (65) Zhu, X.; Caicedo-Dávila, S.; Gehrman, C.; Egger, D. A. Probing the Disorder Inside the Cubic Unit Cell of Halide Perovskites from First-Principles. *ACS Appl. Mater. Interfaces* **2022**, *14* (20), 22973–22981.  
<https://doi.org/10.1021/acsami.1c23099>.
- (66) Wang, B.; Chu, W.; Wu, Y.; Casanova, D.; Saidi, W. A.; Prezhd, O. V. Electron-Volt Fluctuation of Defect Levels in Metal Halide Perovskites on a 100 Ps Time Scale. *J. Phys. Chem. Lett.* **2022**, *13* (25), 5946–5952.

<https://doi.org/10.1021/acs.jpcclett.2c01452>.

- (67) Yang, J.; Li, S. An Atlas of Room-Temperature Stability and Vibrational Anharmonicity of Cubic Perovskites. *Mater. Horiz.* **2022**, *9*(7), 1896–1910. <https://doi.org/10.1039/D2MH00272H>.
- (68) Tyson, T. A.; Gao, W.; Chen, Y.-S.; Ghose, S.; Yan, Y. Large Thermal Motion in Halide Perovskites. *Sci. Rep.* **2017**, *7*(1), 9401. <https://doi.org/10.1038/s41598-017-09220-2>.
- (69) Zelenyak, T. Yu.; Rakhmonov, Kh. R.; Kholmurodov, Kh. T.; Gladyshev, P. P.; Tameev, A. R. Comparative Characterization of Relaxed Organic–Inorganic Hybrid Perovskite Structures Using Molecular Dynamic Simulation and X-Ray Diffraction Data. *High Energy Chem.* **2018**, *52* (5), 433–439. <https://doi.org/10.1134/S0018143918050168>.
- (70) Montero-Alejo, A. L.; Menéndez-Proupin, E.; Hidalgo-Rojas, D.; Palacios, P.; Wahnón, P.; Conesa, J. C. Modeling of Thermal Effect on the Electronic Properties of Photovoltaic Perovskite  $\text{CH}_3\text{NH}_3\text{PbI}_3$ : The Case of Tetragonal Phase. *J. Phys. Chem. C* **2016**, *120* (15), 7976–7986. <https://doi.org/10.1021/acs.jpcc.6b01013>.
- (71) Boukhvalov, D. W.; Zhidkov, I. S.; Akbulatov, A. F.; Kukharensko, A. I.; Cholakh, S. O.; Stevenson, K. J.; Troshin, P. A.; Kurmaev, E. Z. Thermal Effects and Halide Mixing of Hybrid Perovskites: MD and XPS Studies. *J. Phys. Chem. A* **2020**, *124*(1), 135–140. <https://doi.org/10.1021/acs.jpca.9b09653>.
- (72) Zhao, X.-G.; Dalpian, G. M.; Wang, Z.; Zunger, A. Polymorphous Nature of Cubic Halide Perovskites. *Phys. Rev. B* **2020**, *101*(15), 155137. <https://doi.org/10.1103/PhysRevB.101.155137>.
- (73) Fisicaro, G.; La Magna, A.; Alberti, A.; Smecca, E.; Mannino, G.; Deretzis, I. Local Order and Rotational Dynamics in Mixed A-Cation Lead Iodide Perovskites. *J. Phys. Chem. Lett.* **2020**, *11* (3), 1068–1074. <https://doi.org/10.1021/acs.jpcclett.9b03763>.
- (74) Swainson, I.; Chi, L.; Her, J.-H.; Cranswick, L.; Stephens, P.; Winkler, B.; Wilson, D. J.; Milman, V.

- Orientational Ordering, Tilting and Lone-Pair Activity in the Perovskite Methylammonium Tin Bromide,  $\text{CH}_3\text{NH}_3\text{SnBr}_3$ . *Acta Crystallogr. B* **2010**, *66* (4), 422–429. <https://doi.org/10.1107/S0108768110014734>.
- (75) Umebayashi, T.; Asai, K.; Kondo, T.; Nakao, A. Electronic Structures of Lead Iodide Based Low-Dimensional Crystals. *Phys. Rev. B* **2003**, *67* (15), 155405. <https://doi.org/10.1103/PhysRevB.67.155405>.
- (76) Knop, O.; Wasylishen, R. E.; White, M. A.; Cameron, T. S.; Oort, M. J. M. V. Alkylammonium Lead Halides. Part 2.  $\text{CH}_3\text{NH}_3\text{PbX}_3$  (X = Cl, Br, I) Perovskites: Cuboctahedral Halide Cages with Isotropic Cation Reorientation. *Can. J. Chem.* **1990**, *68* (3), 412–422. <https://doi.org/10.1139/v90-063>.
- (77) Onoda-Yamamuro, N.; Matsuo, T.; Suga, H. Calorimetric and IR Spectroscopic Studies of Phase Transitions in Methylammonium Trihalogenoplumbates (II)<sup>†</sup>. *J. Phys. Chem. Solids* **1990**, *51* (12), 1383–1395. [https://doi.org/10.1016/0022-3697\(90\)90021-7](https://doi.org/10.1016/0022-3697(90)90021-7).
- (78) Glaser, T.; Müller, C.; Sendner, M.; Krekeler, C.; Semonin, O. E.; Hull, T. D.; Yaffe, O.; Owen, J. S.; Kowalsky, W.; Pucci, A.; Lovrinčić, R. Infrared Spectroscopic Study of Vibrational Modes in Methylammonium Lead Halide Perovskites. *J. Phys. Chem. Lett.* **2015**, *6* (15), 2913–2918. <https://doi.org/10.1021/acs.jpcclett.5b01309>.
- (79) Yue, S.-Y.; Zhang, X.; Qin, G.; Yang, J.; Hu, M. Insight into the Collective Vibrational Modes Driving Ultralow Thermal Conductivity of Perovskite Solar Cells. *Phys. Rev. B* **2016**, *94* (11), 115427. <https://doi.org/10.1103/PhysRevB.94.115427>.
- (80) Baikie, T.; Fang, Y.; Kadro, J. M.; Schreyer, M.; Wei, F.; Mhaisalkar, S. G.; Graetzel, M.; White, T. J. Synthesis and Crystal Chemistry of the Hybrid Perovskite  $(\text{CH}_3\text{NH}_3)\text{PbI}_3$  for Solid-State Sensitised Solar Cell Applications. *J. Mater. Chem. A* **2013**, *1* (18), 5628–5641. <https://doi.org/10.1039/C3TA10518K>.
- (81) Rebecca, L. W. X.; Burhanudin, Z. A.; Abdullah, M.; Saheed, M. S. M. Structural Changes and Band Gap Tunability with Incorporation of N-Butylammonium Iodide in Perovskite Thin Film. *Heliyon* **2020**, *6* (2),

e03364. <https://doi.org/10.1016/j.heliyon.2020.e03364>.

- (82) Zhou, L.; Neukirch, A. J.; Vogel, D. J.; Kilin, D. S.; Pedesseau, L.; Carignano, M. A.; Mohite, A. D.; Even, J.; Katan, C.; Tretiak, S. Density of States Broadening in CH<sub>3</sub>NH<sub>3</sub>PbI<sub>3</sub> Hybrid Perovskites Understood from Ab Initio Molecular Dynamics Simulations. *ACS Energy Lett.* **2020**, *5*, 2713–2720. <https://doi.org/10.1021/acseenergylett.8b01608>.
- (83) Li, W.; Tang, J.; Casanova, D.; Prezhdo, O. V. Time-Domain Ab Initio Analysis Rationalizes the Unusual Temperature Dependence of Charge Carrier Relaxation in Lead Halide Perovskite. *ACS Energy Lett.* **2018**, *3*, 2713–2720. <https://doi.org/10.1021/acseenergylett.8b01608>.
- (84) Motta, C.; El-Mellouhi, F.; Kais, S.; Tabet, N.; Alharbi, F.; Sanvito, S. Revealing the Role of Organic Cations in Hybrid Halide Perovskite CH<sub>3</sub>NH<sub>3</sub>PbI<sub>3</sub>. *Nat. Commun.* **2015**, *6* (1), 7026. <https://doi.org/10.1038/ncomms8026>.
- (85) Newton, M. D.; Sutin, N. Electron Transfer Reactions in Condensed Phases. *Annu. Rev. Phys. Chem.* **1984**, *35* (1), 437–480. <https://doi.org/10.1146/annurev.pc.35.100184.002253>.
- (86) Prezhdo, O. V.; Rossky, P. J. Evaluation of Quantum Transition Rates from Quantum-Classical Molecular Dynamics Simulations. *J. Chem. Phys.* **1997**, *107* (15), 5863–5878. <https://doi.org/10.1063/1.474312>.
- (87) Jankowska, J.; Prezhdo, O. V. Ferroelectric Alignment of Organic Cations Inhibits Nonradiative Electron–Hole Recombination in Hybrid Perovskites: Ab Initio Nonadiabatic Molecular Dynamics. *J. Phys. Chem. Lett.* **2017**, *8* (4), 812–818. <https://doi.org/10.1021/acs.jpcclett.7b00008>.
- (88) Chen, T.; Chen, W.-L.; Foley, B. J.; Lee, J.; Ruff, J. P. C.; Ko, J. Y. P.; Brown, C. M.; Harriger, L. W.; Zhang, D.; Park, C.; Yoon, M.; Chang, Y.-M.; Choi, J. J.; Lee, S.-H. Origin of Long Lifetime of Band-Edge Charge Carriers in Organic–Inorganic Lead Iodide Perovskites. *Proc. Natl. Acad. Sci.* **2017**, *114* (29), 7519–7524. <https://doi.org/10.1073/pnas.1704421114>.
- (89) Zheng, F.; Tan, L. Z.; Liu, S.; Rappe, A. M. Rashba Spin–Orbit Coupling Enhanced Carrier Lifetime in

- CH<sub>3</sub>NH<sub>3</sub>PbI<sub>3</sub>. *Nano Lett.* **2015**, *15* (12), 7794–7800. <https://doi.org/10.1021/acs.nanolett.5b01854>.
- (90) Fan, Z.; Xiao, J.; Sun, K.; Chen, L.; Hu, Y.; Ouyang, J.; Ong, K. P.; Zeng, K.; Wang, J. Ferroelectricity of CH<sub>3</sub>NH<sub>3</sub>PbI<sub>3</sub> Perovskite. *J. Phys. Chem. Lett.* **2015**, *6* (7), 1155–1161. <https://doi.org/10.1021/acs.jpcllett.5b00389>.
- (91) Chu, W.; Saidi, W. A.; Zhao, J.; Prezhdo, O. V. Soft Lattice and Defect Covalency Rationalize Tolerance of B-CsPbI<sub>3</sub> Perovskite Solar Cells to Native Defects. *Angew. Chem. Int. Ed.* **2020**, *59* (16), 6435–6441. <https://doi.org/10.1002/anie.201915702>.
- (92) Chu, W.; Zheng, Q.; Prezhdo, O. V.; Zhao, J.; Saidi, W. A. Low-Frequency Lattice Phonons in Halide Perovskites Explain High Defect Tolerance toward Electron-Hole Recombination. *Sci. Adv.* **2020**, *6* (7), eaaw7453. <https://doi.org/10.1126/sciadv.aaw7453>.
- (93) Cohen, A. V.; Egger, D. A.; Rappe, A. M.; Kronik, L. Breakdown of the Static Picture of Defect Energetics in Halide Perovskites: The Case of the Br Vacancy in CsPbBr<sub>3</sub>. *J. Phys. Chem. Lett.* **2019**, *10* (16), 4490–4498. <https://doi.org/10.1021/acs.jpcllett.9b01855>.
- (94) Shockley, W.; Read, W. T. Statistics of the Recombinations of Holes and Electrons. *Phys. Rev.* **1952**, *87* (5), 835–842. <https://doi.org/10.1103/PhysRev.87.835>.